CROSS: Cross-Domain Residual-Optimization-Based Structure Strengthening Reconstruction for Limited-Angle CT

Dianlin Hu, Yikun Zhang, Guotao Quan, Jun Xiang, Gouenou Coatrieux, Shouhua Luo, Jean-Louis Coatrieux, Xu Ji, Hongbin Han, Yang Chen

CROSS: Cross-domain Residual-Optimization Based Structure Strengthening Reconstruction for Limited-Angle CT

Dianlin Hu, Yikun Zhang, Guotao Quan, Jun Xiang, Gouenou Coatrieux, *Senior Member, IEEE*, Shouhua Luo, Jean-Louis Coatrieux, *Life Fellow, IEEE*, Xu Ji, Hongbin Han, Yang Chen, *Senior Member, IEEE*

***Abstract*—Limited-angle CT is an effective way for practical scenario due to its flexibility in various complex scanning conditions. However, incomplete projection data will lead to severe wedge artifacts and degraded images, which significantly lower the diagnostic values. To overcome this problem, we propose a novel method termed Cross-domain Residual-Optimization Based Structure Strengthening (CROSS) Reconstruction for limited-angle CT. The proposed CROSS framework consists of three steps, which are conducted on the image domain and measurement domain alternatively. Differing from traditional dual-domain-based algorithms, our CROSS method not only regularizes the reconstruction results on the image space but also the residual-error space, which boosts organ recovery where the area has a larger attenuation coefficient. Besides, the structure-strengthening network is adopted to enhance tissue preservation. Simulated and preclinical datasets are conducted to evaluate the proposed CROSS method. Experiments show that the proposed framework could produce a better performance in artifact removal and edge preservation.**

***Index Terms*—Cross-domain based processing, residual-error space regularization, structure enhancement network, data consistency, limited-angle CT reconstruction.**

This work was supported in part by the State Key Project of Research and Development Plan under Grants 2022YFC2408500 and 2022YFC2401600, in part by the National Natural Science Foundation of China under Grant T2225025, in part by the Key Research and Development Programs in Jiangsu Province of China under Grant BE2021703 and BE2022768. (*Corresponding authors: Xu Ji, Hongbin Han*).

This work involved human subjects or animals in its research. The authors confirm that all human/animal subject research procedures and protocols are exempt from review board approval.

Dianlin Hu, Yikun Zhang, Xu Ji and Yang Chen are with the Laboratory of Image Science and Technology, the School of Computer Science and Engineering, Southeast University, Nanjing 210096, China (e-mail: dianlin@seu.edu.cn; yikun@seu.edu.cn; xuji@seu.edu.cn; chenyang.list@seu.edu.cn).

Guotao Quan is with the CT RPA Department, United Imaging Healthcare Limited Company, Shanghai 201807, China (e-mail: guotao.quan@unitedimaging.com).

Jun Xiang is with the X-Ray Department, United Imaging Healthcare Limited Company, Shanghai 201807, China (e-mail: Jun.xiang@unitedimaging.com).

Gouenou Coatrieux is with the IMT Atlantique, Inserm, LaTIM UMR1101, Brest 29000, France (e-mail: gouenou.coatrieux@telecom-bretagne.eu).

Shouhua Luo is with the Department of Biomedical Engineering, Southeast University, Nanjing 210096, China (e-mail: luoshouhua@seu.edu.cn).

Jean-Louis Coatrieux is with Inserm Emeritus Research Director at LTSI (U1099, Rennes, France) and Professor at the Computer Science Department of Southeast University, Nanjing, China.

Hongbin Han is with the Institute of Medical Technology, Peking University Health Science Center, Beijing 100191, China, and with the Department of Radiology, Peking University Third Hospital, Beijing 100191, China (e-mail: hanhongbin@bjmu.edu.cn).

I. Introduction

X-RAY Computed Tomography (CT) has been widely used in medical diagnosis, industrial non-destructive detection, and security checks [1]. However, CT images will encounter severe noise and artifacts in non-ideal environments. Particularly, in the practical scenarios [2-4], the measurements cannot be collected from the full-angle range. For example, in radiation therapy (RT), cone-beam computed tomography (CBCT) can be used for patient setup and dose calculation [5]. However, CBCT takes a long time (usually 60s) to rotate one circle, which may lead to motion artifacts caused by patient or organ movements. Limited-angle scanning mode can accelerate the acquisition time and proportionally reduce the radiation dose. Consequently, the obtained limited-angle projection data will result in degraded images with severe wedge artifacts and significantly lower practical values. To tackle this problem, many advanced reconstruction methods have been proposed, which can be divided into four categories: analytical methods, iterative (IR) optimization methods, deep learning (DL)-based methods, and deep iterative methods.

Filtered Back Projection (FBP) is a classical analytical method and has been commonly employed in CT reconstruction. FBP can fast provide high-quality images when the projection data is complete and noiseless. Nevertheless, for limited-angle CT, FBP will introduce shadow artifacts and lose tissue details.

To guarantee the consistency between reconstruction images and projection data and further improve the performance of FBP, numerous IR methods have been proposed for limited-angle CT [6]. Later, various prior regularizations were introduced into CT imaging to improve the performance in artifact removal and tissue restoration [7, 8]. Considering the sparse property of image gradients, Sidky *et al.* applied the total variation (TV) minimization to limited-angle CT and demonstrated improvements compared to the algebraic reconstruction technique (ART) [9]. Further, noticing the isotropic in TV was unfit for limited-angle CT, Chen *et al.*

developed an anisotropic TV (TV) based IR method [10] for better edge preservation and wedge artifact reduction. To more effectively utilize image sparsity, Wang *et al.* incorporated the reweighted technique into ATV (RwATV) [11]. Experiments showed that RwATV could generate better reconstructions with clearer structures, sharper edges, and fewer artifacts. However, RwATV maybe fail to eliminate large streaks because it was scale-dependent. Therefore, the scale-space ATV was researched to reduce the streak artifacts at different scales [12]. L_0-norm was another important prior constraint in medical imaging and it can provide a more sparse solution than TV [13]. For example, to overcome the weakness of TV in over-smoothing low-contrast structures, Sun *et al.* attempted to introduce L_0-norm optimization into the IR method and achieved obvious promotion [14]. Then, Wang *et al.* paid attention to punishing the wavelet coefficients based on the L_0-norm and outperformed classical CT reconstruction in metal artifact suppression [15]. To better improve the performance in feature restoration, Xu *et al.* combined the L_0-norm and dictionary learning (L_0DL) for limited-angle CT. Both simulated and preclinical datasets claimed the proposed L_0DL generated high-quality images with more clear structures [16]. In addition, non-local similarity [17], low-rank [18], and sparse representation [19, 20] were also commonly used as prior knowledge in IR algorithms for CT reconstruction and achieved competitive results. Although prior-regularized IR methods can improve CT images, they had several shortcomings, including high computational cost, sensitive hyper-parameter settings, and hand-crafted regularization terms.

Recently, DL-based methods have been successfully applied to the field of medical imaging [21-23]. Especially, convolutional neural network (CNN)-based methods brought more promising results than traditional reconstruction images [24-27]. Aided by the powerful feature extraction ability of the CNN model, Gu *et al.* directly predict the artifacts in the wavelet domain from the degraded images and performed well in artifact reduction [28]. Similarly, Li *et al.* proposed an inpainting network to restore the missing projection data for limited-angle scanning. Then, the classical FBP or IR methods were employed to reconstruct CT images from the recovered projection data. Experiments stated that serious artifacts can be effectively reduced [29]. Unlike the above single-domain-based methods, Anirudh *et al.* adopted the generative adversarial network to directly map the incomplete fan-beam sinogram data into the CT images and obtained impressive results [30]. Meanwhile, Würfl *et al.* explored an FBP-type algorithm with a novel back-projection layer for cone-beam geometry to improve the calculating efficiency. Evaluations demonstrated this scheme outperformed analytical methods [31]. Innovatively, Huang *et al.* introduced a data-consistent artifact reduction (DCAR) method based on the deep learning prior, which first inpainted the missing projection data and then iteratively improve the reconstruction images [32] with IR methods. To strengthen edge preservation, Hu *et al.* proposed a multi-stage reconstruction framework (SPECIAL) for limited-angle CT. Simulated and real experiments suggested that the SPECIAL method outperformed existing competitive algorithms in artifact removal and detail recovery [33].

Further, dual-domain-based methods have attracted great attention because of their superior performance. By jointly constraining the projection data and image data, these methods outperform single-domain-based methods. For example, to make full use of complementary correlations between the image domain and projection domain, a hybrid domain network (hdNet) was developed for limited-angle CT. Experiments suggested that the hdNet works well in eliminating artifacts [34]. Besides, Jiao *et al.* developed an intelligent back-projection network (iBP-Net) for CT reconstruction and could provide visually improved results [35]. And Zhou *et al.* employed the dual-domain method for metal artifact reduction in low-dose CT [36]. Considering the instabilities of deep learning methods in medical imaging, Wu *et al.* specifically designed an Analytic compressed iterative deep (ACID) method to stabilize the deep tomography reconstruction [37, 38]. Based on ACID, Wu *et al.* integrated the residual-domain processing technique into the dual-domain method for sparse-view CT and works well in artifact reduction and detail preservation [39, 40].

According to mentioned works, both IR methods and DL-based methods were effective to improve image quality. Therefore, deep iterative reconstruction algorithms, which combined IR optimization and deep learning prior, have been researched for image restoration [41, 42]. By implementing the differentiable forward-backward operator, Cheng *et al.* developed an unrolled method (FSR-Net) to jointly reconstruct a high-quality CT image and its corresponding full-view projection data. FSR-Net deployed the regularization both on the image domain and projection domain and outperformed existing variational and DL-based methods [43]. Next, to improve the regularization capacity of deep prior and enhance data consistency, Zhou *et al.* employed the dense spatial-attention network with a specialized data fidelity layer for limited-angle CT reconstruction. Experiments implied that [44] was able to generate promising results for major lesions. Based on [44], Sam's Net was further investigated to utilize the hybrid-domain-based method as the backbone and lead to improvements in stability and robustness [45]. Even though [43-45] represented state-of-the-art methods, they cannot directly be applied to cone-beam CT due to memory limitations. Hence, some deep iterative methods with an offline scheme have been proposed. To accelerate the convergence speed of IR methods, Wang *et al.* adopted several DL models as regularization functions to improve the intermediate reconstruction results [46]. As a result, [46] performed better in edge preservation and artifact reduction. Besides, to solve the generalization of deep priors in the iterative process, Hu *et al.* designed a residual-space-based CNN model embedded in the IR method and make a significant promotion in detail restoration [47].

Nevertheless, [46, 47] needed a much longer time than other competitive methods due to the complex computational iterative procedure. Consequently, this paper proposes a

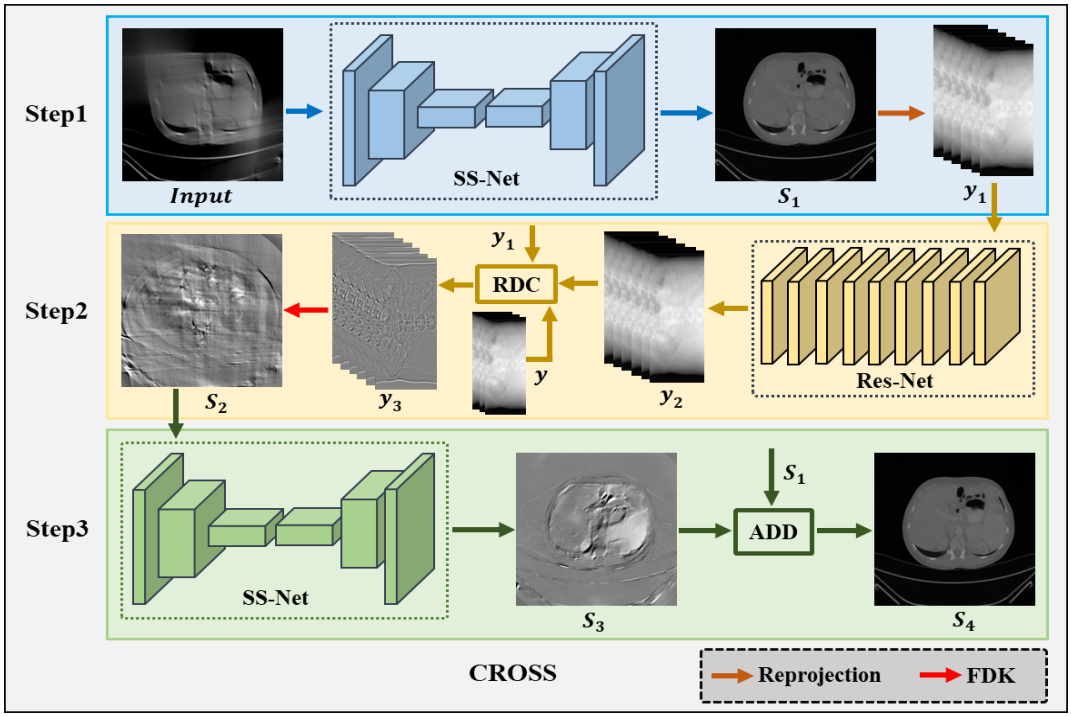

Fig. 1. The flowchart of the CROSS framework.

Cross-domain Residual-Optimization based Structure Strengthening (CROSS) framework for limited-angle CT reconstruction. The proposed CROSS method consists of three steps, which alternatively perform the CNN model on the image domain and projection domain. Specifically, in the first step, the structure strengthening network (SS-Net) is adopted to remove the artifacts and preserve the textures. Next, the missing projection data can be obtained from the results in the first step according to [32]. For the purpose of data consistency improvement, a residual network (ResNet) is applied to boost restored projection data. Different from the last step in [33], the proposed CROSS utilizes the SS-Net on the residual error map rather than the CT images, which could improve the restoration accuracy in the areas that have the larger attenuation coefficients. Compared to deep iterative methods [44, 47], the CROSS method can be applied to cone-beam CT reconstruction with less computational cost and provides competitive results simultaneously. Experiments based on the simulated and real datasets validate that the proposed CROSS method performs well in edge preservation, detail restoration, and artifact removal.

The rest of this paper is organized as follows. Section II introduces the workflow of the proposed CROSS framework and the details of the neural network used in this work. Section III gives the experimental results and analysis of the different components in CROSS. In section IV, we will discuss some related issues and make a plan for the next work.

II. Methodology

A. CROSS Framework

To reconstruct high-quality images similar to deep iterative methods [43, 44, 47], but with lower computational cost, a multi-step method termed CROSS is proposed. The CROSS framework consists of three steps (as shown in Fig. 1), which alternatively employ the CNN models on the image space and projection space to gradually boost the CT images.

In the first step, a novel structure-strengthening network (SS-Net) is adopted in the image domain to remove the artifacts and restore most of the tissue details. Specifically, SS-Net takes the degraded images reconstructed from limited-angle projection data $\boldsymbol{y}$ using the FDK algorithm as input and generates high-quality images $\boldsymbol{S_1}$. Unlike [28, 33, 48], SS-Net designs a structure-enhanced branch, which can lead to impressive results in detail restoration.

Although the $\boldsymbol{S_1}$ obtained at the first step has satisfactory visual results, but it may fail to accurately reconstruct the areas that have larger attenuation coefficients. Therefore, the data consistency operation is employed to further improve $\boldsymbol{S_1}$. In particular, the projection data $\boldsymbol{y_1}$ reprojected from the $\boldsymbol{S_1}$ is input into a normal ResNet and produces an improved full-view projection data $\boldsymbol{y_2}$. Next, the residual data consistency (RDC) is utilized to evaluate the difference $\boldsymbol{y_3}$ between $\boldsymbol{S_1}$ and the available projection $\boldsymbol{y}$. Differing from traditional data consistency [32, 44], RDC focuses on the assessment of error maps on the projection domain and can provide superior results.

In the last step, an error image $\boldsymbol{S_2}$ is first reconstructed from the error sinogram $\boldsymbol{y_3}$. Despite the wedge artifacts, it contains high-frequency information between the $\boldsymbol{S_1}$ and the ground truth, which can be easily restored for $\boldsymbol{S_1}$. Hence, the SS-Net is used again to correct the $\boldsymbol{S_2}$. Then the final results $\boldsymbol{S_4}$ can be got by adding $\boldsymbol{S_3}$ and $\boldsymbol{S_1}$.

In general, the key point of the CROSS method is to respectively promote the reconstructed result in the residual image space and projection space, which is beneficial to recover bigger organs with high Hounsfield units (HU).

B. *Structure Strengthening Network*

To better reconstruct images for limited-angle CT, the SS-Net is employed in the image domain, whose architecture is shown in Fig. 2. SS-Net has three branches, which are the image restoration sub-network, structure-enhanced sub-network [49-51], and feature fusion sub-network, respectively.

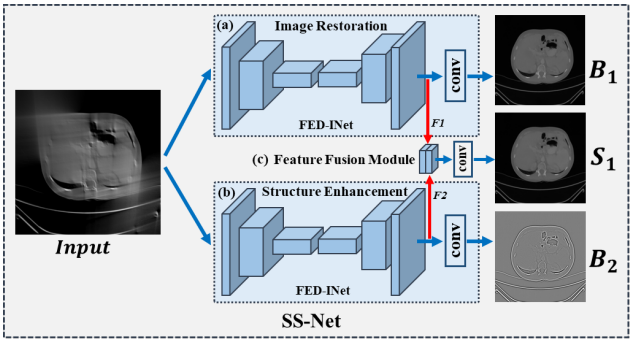

Fig. 2. The proposed SS-Net architecture.

The image restoration sub-network (IRS-Net) (as shown in Fig. 2(a)) adopts the FED-INet as the backbone [47], which employs the asymmetric convolutional module (ACM) to improve the feature extraction and has been effectively validated for tissue restoration. IRS-Net is a classical image-domain-based method that takes the FDK reconstruction images as input and generates high-quality images $\boldsymbol{B_1}$ with most structures and less artifacts. So, IRS-Net holds the low-frequency information of CT images.

Dissimilarly, the structure enhancement sub-network (SES-Net) (as illustrated in Fig.2 (b)) attempts to preserve the texture information contained in the CT images. SES-Net also uses the FED-INet as the backbone and inputs the FDK results but outputs the structure details $\boldsymbol{B_2}$. Consequently, the high-frequency information of the CT images is stored in the feature maps of the SES-Net.

Since IRS-Net and SES-Net separately possess the low- and high-frequency components of the CT images, they can be further improved by fusing their feature maps. As depicted in Fig. 2(c), the feature fusion module (FFM) concatenates the feature maps together, which are extracted from the IRS-Net and SES-Net respectively, and brings improvements over $\boldsymbol{S_1}$ in edge preservation.

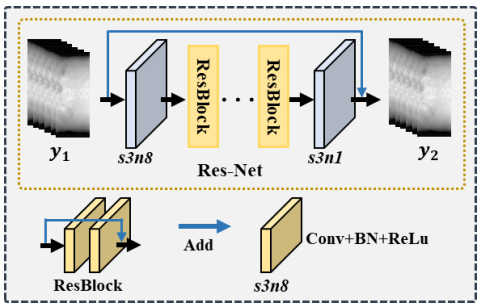

Fig. 3. The proposed ResNet architecture.

C. *ResNet*

For better reconstructing high-resolution projection data, the ResNet is utilized, whose architecture is demonstrated in Fig. 3. It consists of eight ResBlocks and each ResBlock has a residual connection to avoid vanishing or exploding gradients [52]. Besides, ResNet also adopts the global residual connection to accelerate convergence and stable training [53].

D. *Residual Data Consistency*

Data consistency is a widely used constraint in medical imaging [44, 54], which can guarantee the worst-case performance of reconstruction methods [55]. The classical data consistency can be rewritten as follows [32].

$$y_3 = y \oplus y_2 \tag{1}$$

where $\boldsymbol{y}$ is the available limited-angle projection data, $\boldsymbol{y_2}$ represents improved high-resolution projection data processed by the ResNet (as indicated in Fig. 1) and $\oplus$ stands for the replacement operation which copies the $\boldsymbol{y}$ and replaces the corresponding part of $\boldsymbol{y_2}$ with $\boldsymbol{y}$. Then a more accurate projection data $\boldsymbol{y_3}$ can be used for subsequent operations [32, 44].

To improve tissue preservation, the RDC is investigated and its formulation is as follows.

$$y_3 = y \oplus y_2 - y_1 \tag{2}$$

where $y_1 = \boldsymbol{A}\boldsymbol{S}_1$, A is the projection operation. Unlike Eq. (1), RDC aims to evaluate the difference between the $\boldsymbol{S_1}$ and the ground truth in the projection domain, which can improve the performance of $\boldsymbol{S_1}$ in high-attenuation regions.

E. *Perceptual Loss*

Perceptual loss (PL) is the widely used tool to minimize the distance between two images in feature space rather than pixel-wise similarity. In the application of medical imaging, PL can generate more tissue details and a better visual appearance [56]. The definition of PL is given as:

$$L_{PL}(I, gt) = \sum_{i=1}^{N} \|\Psi_i(I) - \Psi_i(gt)\|_F^2 \tag{3}$$

where I is the reconstructed image and gt indicates the ground truth. Ψ_i represents the feature projector [47]. In this work, the output of the 2nd, 4th, 6th, 9th, and 12th convolutional layer of VGG-16 [57] as the feature extractor Ψ_i.

F. *Texture Extraction*

CNN-based models tend to blur images [33], therefore, to enhance the CNN models in edge preservation, texture extraction (TE) is utilized in the CROSS framework. The TE can be expressed as follows.

$$H(I) = I - F(I, g) \tag{4}$$

where $g \sim N(\mu, \sigma^2)$ follows the gaussian distribution with the mean value μ and standard variation σ, and F is the filtering operation. Using Eq. (4), the textures and details of the image I can be obtained (as observed in $\boldsymbol{B_2}$ of Fig. 2(b)). Texture extraction was also used in [33, 47], and these texture extractions directly perform on reconstructed images to explicitly enhance detail preservation. However, in our method, the texture extraction is to extract high-frequency feature maps

with an implicit approach and then feed them into the final results.

G. Loss Function

There are three neural networks Φ_1, Φ_2 and Φ_3 for the three steps in CROSS, respectively.

In the first stage of CROSS, the cost function of Φ_1 is described as:

$$\Phi_1 = \underset{\Phi_1}{\operatorname{argmin}} \left\| \Phi_{1_{\mathrm{b}1}}(I_D) - I_{ND} \right\|_F^2 + \left\| \Phi_{1_{\mathrm{b}2}}(I_D) - H(I_{ND}) \right\|_F^2 + \left\| \Phi_{1_{\mathrm{b}3}}(I_D) - I_{ND} \right\|_F^2 + \lambda_1 \cdot L_{PL}(\Phi_{1_{\mathrm{b}3}}(I_D), I_{ND}) \quad (5)$$

where I_D is the limited-angle reconstructed image, I_{ND} indicates the reference image reconstructed from the full-view projection data. $\Phi_{1_{\mathrm{b}1}}$, $\Phi_{1_{\mathrm{b}2}}$, and $\Phi_{1_{\mathrm{b}3}}$ stands for the three sub-networks in Fig. 2, λ_1 represents the hyperparameter to balance different terms in Eq. (5).

In the second stage, the objective function of Φ_2 is:

$$\Phi_2 = \underset{\Phi_2}{\operatorname{argmin}} \| \Phi_2(y_1) - y_{ND} \|_F^2 \quad (6)$$

where y_{ND} is the full-view projection data.

For the Φ_3, it has the same optimization function with Φ_1 but with different input and reference images.

$$\Phi_3 = \underset{\Phi_3}{\operatorname{argmin}} \left\| \Phi_{3_{\mathrm{b}1}}(S_2) - R_{ND} \right\|_F^2 + \left\| \Phi_{3_{\mathrm{b}2}}(S_2) - H(R_{ND}) \right\|_F^2 + \left\| \Phi_{3_{\mathrm{b}3}}(S_2) - R_{ND} \right\|_F^2 + \lambda_2 \cdot L_{PL}(\Phi_{3_{\mathrm{b}3}}(S_2), R_{ND}) \quad (7)$$

where $S_2 = FDK(y_3)$, $R_{ND} = I_{ND} - S_1$, and λ_2 is another hyperparameter to control the trade-off in all terms. After training the Φ_1, Φ_2 and Φ_3, the proposed CROSS can gradually improve the images with alternative image domain and projection domain processing.

III. Experiments

In this work, all the experiments were conducted on a PC with CPU Inter(R) Xeon E5-2683 and GPU NIVIDA GTX TITAN. The hyper-parameters λ_1 and λ_2 in Eqs. (5) and (7) were set to 0.001 and 0.001, respectively. All the parameters of the three networks Φ_1, Φ_2 and Φ_3 were updated using the Adam algorithm [58]. Noting that these three networks were dependent and needed to be trained one by one. The learning rate was initially set to 10^{-3} and linearly decreased to $1e^{-5}$ within 50 epochs. To evaluate the proposed CROSS framework, five reconstruction methods were treated as comparisons, including the FDK algorithm (Ramp-filter), TV [59], DDNet [48], MSWDNet [28], and DCAR[32]. Specifically, DDNet, MSWDNet, and DCAR were implemented in the TensorFlow framework with Python language. FDK and TV were conducted by MATLAB 2018a. Besides, we choose the peak single-to-noise ratio (PSNR), and structural similarity index (SSIM) [60] as the quantitative evaluations.

A. Simulated Data Results

The images of simulated experiments were downloaded from The Cancer Imaging Archive (TCIA). In this work, we adopted cone-beam geometry to evaluate different reconstruction methods for limited-angle CT. The geometry parameters were as follows. The source-to-detector distance was 100 cm and the source-to-axial distance was 50 cm, respectively. The detector size was 900×400 and each element covered an area of 1.5×1.5 mm^2. For one circle, there were 960 views were collected. The volume was reconstructed with 512×512×200 and each voxel was 0.9×0.9×0.9 mm^3. It was worth noting that FDK will lead to cone-beam artifacts when the reconstructed slice is far away from the central slice. To overcome this issue, we only selected the middle 120 slices in the entire volume. That means each 3D volume in the following experiments only has a size of 512×512×120. Particularly, there were 9200 2D images with the size of 512×512 selected from twenty-one patients in the TCIA dataset to simulate the cone-beam geometry as described in this section to generate the training dataset. Then, another 1000 2D images of the same size from different three patients were used to generate the validation dataset. Last, 1200 2D images selected from another three patients were utilized to generate the testing dataset. Specifically, the images from training, validation, and testing datasets belonged to different patients. The FDK algorithm was used to reconstruct the reference images from the full-sampled projection data. Two scanning angular ranges [0, 90°] and [0, 110°] were performed to assess different methods. For the DL-based methods, the input and output were 2D slices extracted from the 3D volumes. During the training phase, the patch-based scheme was adopted. Each patch had a size of 128×128 extracted from the 2D slices with the stride step of 64 and the batch size was 16. In the testing phase, the image with the size of 512×512 was directly inputted into the trained model and outputted generated result.

Table I lists the average quantitative results of reconstructed images with the scanning angular ranges of [0,90°] and [0,110°]. In Table I, it can be noticed that the analytical algorithm FDK produces the worst scores, which claims that the performance of the analytical algorithm can be affected greatly in all methods when the projection data is incomplete. Aided by the image gradient minimization and iterative forward-backword correction, TV achieves better assessments than FDK but still fails to provide competitive results, which implies that traditional methods cannot reconstruct satisfactory results with incomplete measurement data. Because of the powerful feature extraction ability, DL-based methods get better evaluation scores than traditional methods in all scanning angular ranges. Compared to MSWDNet, DDNet brings at least 0.7 dB promotion in terms of PSNR, which claims that the network with a more complex architecture may improve reconstructed results. Although DCAR gets worse scores in PSNR than DDNet, it performs well in SSIM, which means the image content provided by the DCAR is closer to the reference image due to the data consistency constraint. Notably, the proposed CROSS framework gains the best evaluations of all methods, which states the effectiveness of the multi-domain-based processing.

To further evaluate the performance visually of various algorithms, Fig. 4 illustrates the reconstruction results and the corresponding regions-of-interests (ROIs) of FDK, TV,

Table I
QUANTITATIVE EVALUATIONS FOR THE SIMULATED DATASET

Range	Metric	FDK	TV	MSWDNet	DDNet	DCAR	CROSS
[0,90°]	PSNR	15.98	24.00	35.70	36.40	36.34	**37.45**
	SSIM	0.5135	0.7795	0.9535	0.9565	0.9589	**0.9679**
[0,110°]	PSNR	17.22	25.74	36.56	37.52	37.37	**38.50**
	SSIM	0.5368	0.8144	0.9587	0.9610	0.9613	**0.9738**

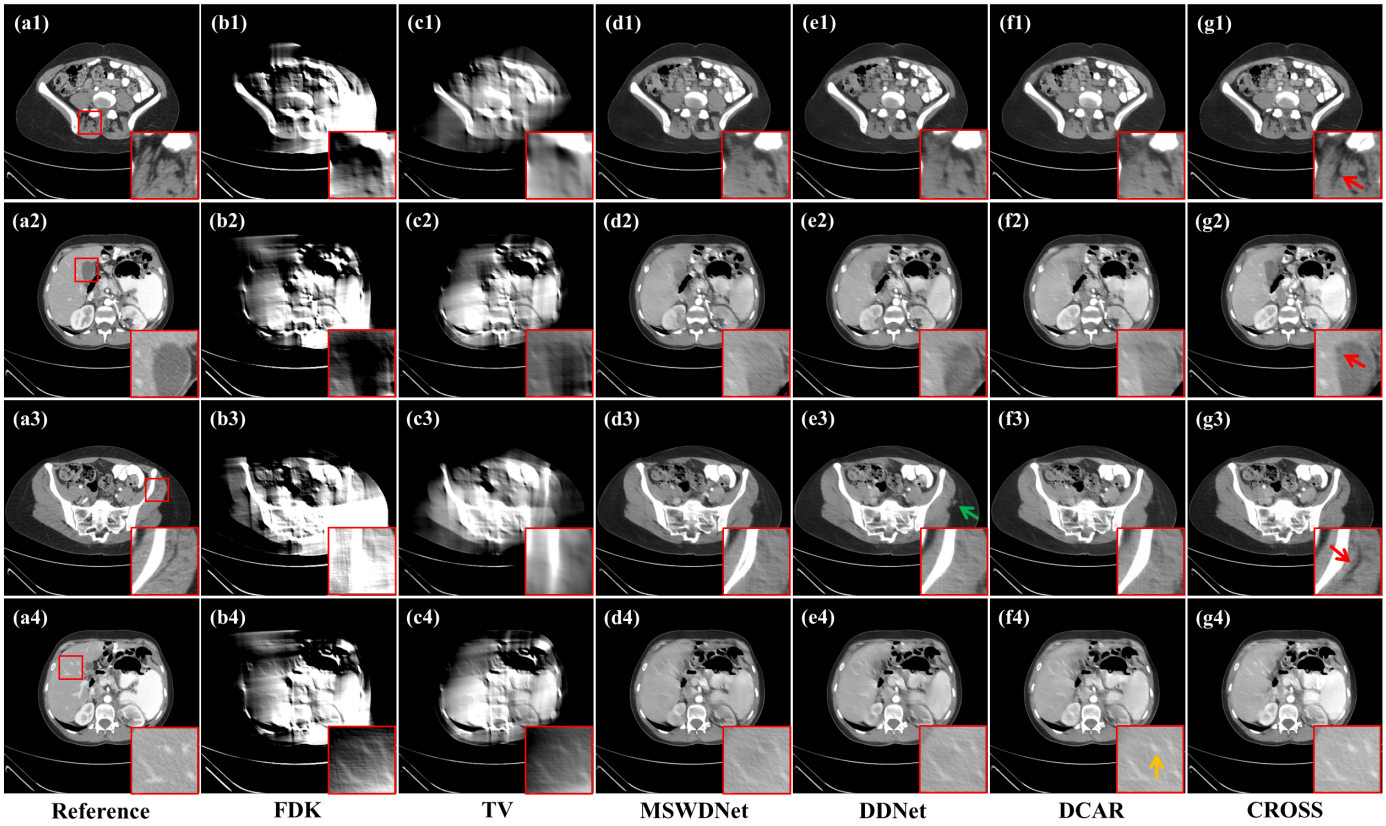

Fig. 4. Simulated dataset reconstruction results with scanning angular angle 110°. And different rows represent different slices. The display window is [-160, 240].

MSWDNet, DDNet, DCAR, and CROSS methods with the scanning angular range of 110°. From Fig. 4(b1)-(b4), it can be seen that FDK introduces severe wedge artifacts, and the tissue and lesion become hard to be recognized. Benefiting from the minimization of image gradients, TV outperforms FDK in artifact removal (as shown in Fig. 4(c1)-(c4)). Nevertheless, most diagnostic information in TV reconstructions is still missing, which exposes the defects of traditional methods when the projection data is incomplete. Assisted by a large number of pairs of training samples and deep convolutional layers, the CNN-based model could exploit the essential features contained in the CT images. Certainly, DL-based algorithms achieve superior performance over traditional methods. Specifically, the image-domain-based methods MSWDNet and DDNet can suppress wedge artifacts and restore tissues and details as demonstrated in Fig. 4(d1)-(e4). This confirms the effectiveness of image-domain-based methods for medical imaging. Further, DCAR could boost post-processing methods in tissue restoration (as pointed out by the yellow arrow in Fig.4 (f4)). Also, it can eliminate the fake structure induced by the DDNet (as indicated by the green arrow in Fig. 4(e3)). This is because that DCAR is an IR-based method and can promote reconstructed results via iterative optimization. It is worth noting that the proposed CROSS method generates more visually improved images than other competitive DL-based methods. Particularly, CROSS is able to preserve subtle details (as observed by the red arrows in Fig. 4(g1)(g3)) and clear organ boundaries (as shown by the red arrow in Fig. 4(g2)).

Fig. 5 exhibits the reconstruction results with the scanning angular range of 90° to probe the performance of different methods with a smaller scanning angular range. Compared to Fig. 4(b1)-(c4), FDK and TV lead to worse reconstruction results with the scanning angular range of 90° (as depicted in Fig. 5(b1)-(c4)). These imply that the performance of traditional methods is significantly influenced by the completeness of projection data. From Fig. 5(d1)-(g4), it can be noted that DL-based methods promote the FDK and TV in artifact removal and tissue restoration. Similar to Fig. 4, MSWDNet and DDNet successfully recover most details and reduce artifacts. Moreover, they can produce more clear tissues than DCAR (as illustrated by the yellow arrows in Fig. 5(d3)(e2)), which is opposite to the phenomena in Fig. 4. This states that DCAR relies on the projection data, and the smaller the scanning angular range, the worse the performance. In contrast to the DCAR method, the proposed CROSS is quite robust to different scanning angular ranges and still provides

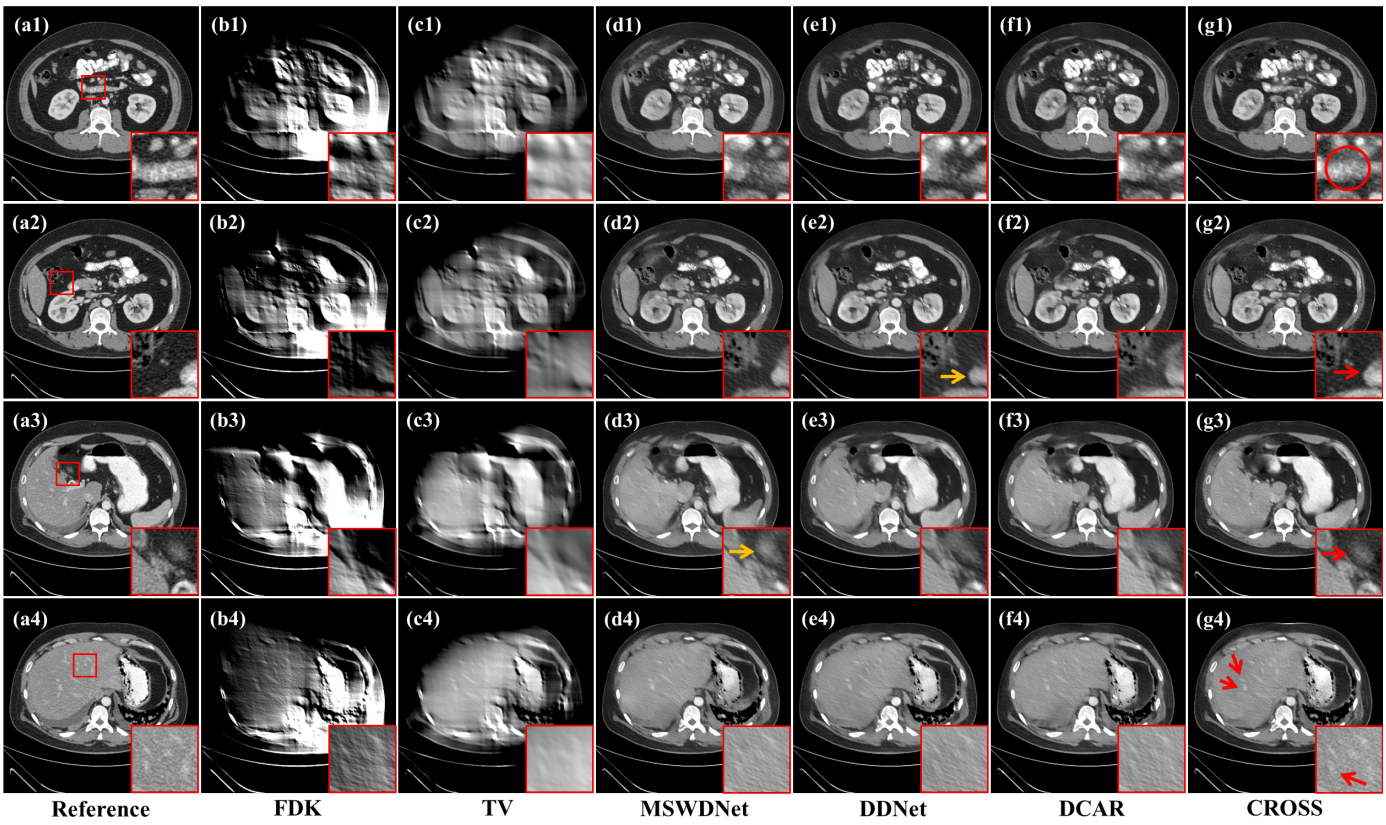

Fig. 5. Simulated dataset reconstruction results with scanning angular angle 90°. And different rows represent different slices. The display window is [-160, 240].

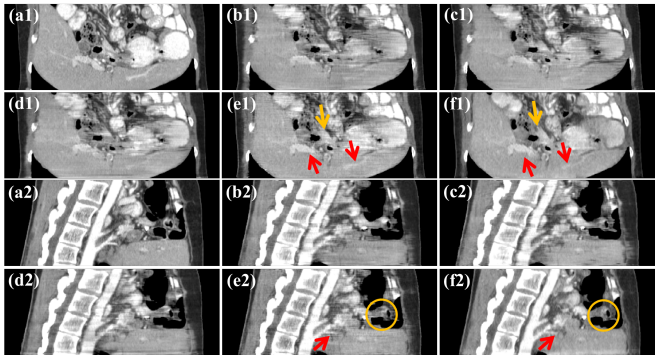

Fig. 6. Selected coronal views and sagittal from the simulated dataset with scanning angular range of 90°. (a1)-(f1) Coronal views of reference, MSWDNet, DDNet, DCAR, CROSS, and 3D-CROSS methods. (a2)-(f2) Sagittal views of reference, MSWDNet, DDNet, DCAR, CROSS, and 3D-CROSS methods. The display window is [-140, 240] HU.

high-quality images with clear edges (as implied by the red arrows in Fig. 5(g2)(g3)) and accurate features (as marked by the red circle and arrow in Fig. 5(g1)(g4)).

Fig. 6 illustrates the selected coronal and sagittal views from the reconstructed CT volumes of the simulated dataset to further evaluate the visual performance of different reconstruction methods. As shown in Fig. 6, all the DL-based methods can reduce most artifacts and preserve the most of tissue features. More specifically, our proposed CROSS framework works well in detail restoration (as suggested by the red arrows in Fig. 6(e1)(e2)). However, the proposed method leads to obvious horizontal artifacts at different slices (as pointed by the yellow arrow and circle in Fig. 6(e1)(e2)). This is because all the reconstructed results are 3D images but the proposed method processes them slice by slice, which ignores the relationship between adjacent slices in the z-axis direction. To solve this problem, the proposed CROSS method is extended to a 3D version (3D-CROSS) that takes the 3D images as input. As observed in Fig. 6(f1)(f2), the 3D-CROSS successfully suppresses the horizontal artifacts. More results of 3D-CROSS can be found in the supplementary material.

B. Real Dataset Results

To further investigate different reconstruction methods for limited-angle CT, real mice dataset experiments were conducted. Again, the cone-beam scanning model was adopted and its configuration is as follows. The tube was Hamamatsu L9421-02 and the detector was Dexela 1512, respectively. The tube voltage was 60 kV and the current was 130 μA. The size of the detector was 944×768 and each element represented 0.072×0.072 mm^2. The distance between the source and the detector was 44 cm and the distance between the source and the object was 22 cm, respectively. 1000 projections were collected via 360° as the full-sampled measurement data. The reconstructed 3D volume was $872 \times 872 \times 600$ and each voxel covered the area of $0.072 \times 0.072 \times 0.072$ mm^3. There were four mice performed for this work. Specifically, two mice (1200 images) were used as the training dataset, one mouse (600 images) was used as the validation dataset and the rest (600 images) was used as the training dataset. Similar to the previous section, we only reconstruct the central 600 slices for each mouse to alleviate the cone-beam artifacts. The FDK algorithm was adopted to reconstruct the reference images from the full-sampled projection data. One scanning angular range

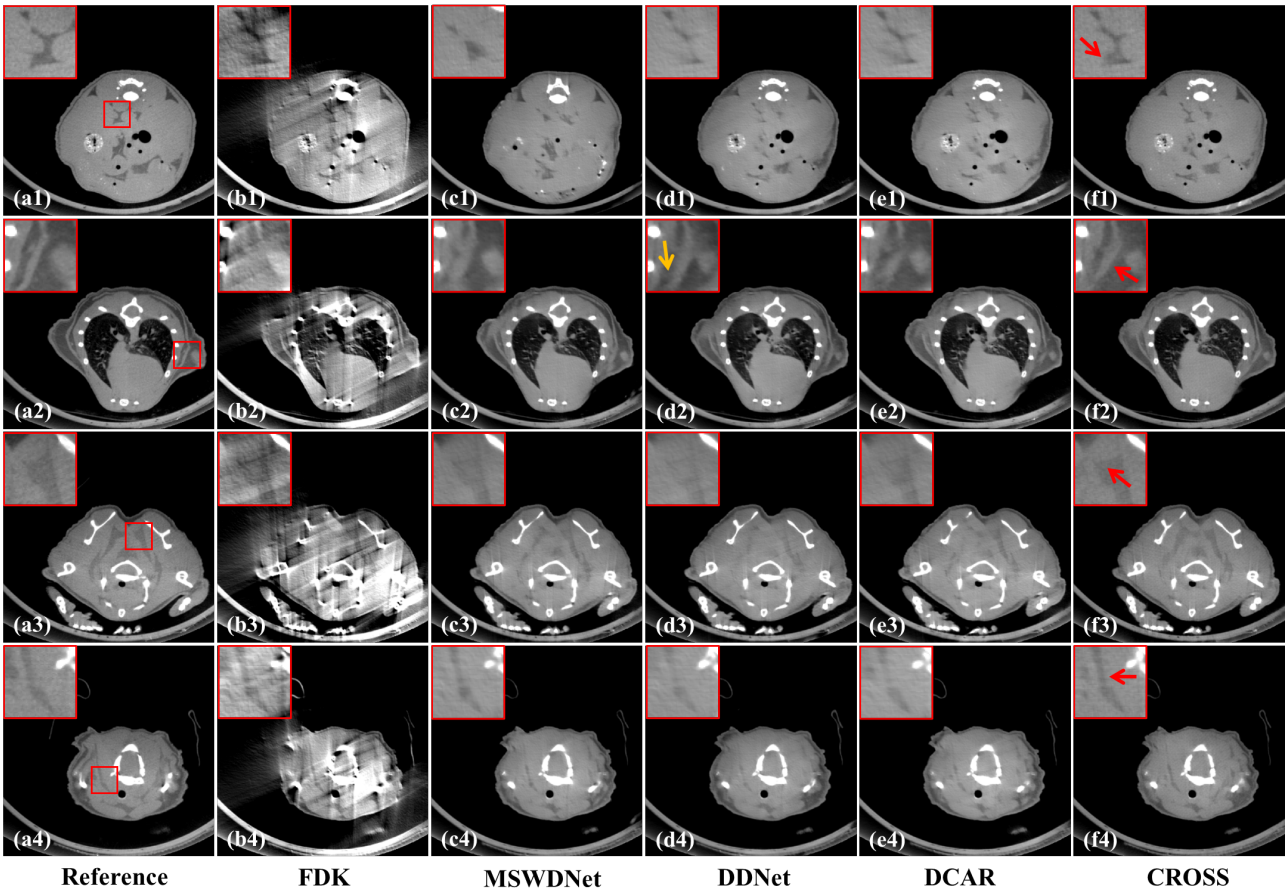

Fig. 7. Real mice dataset reconstruction images with a scanning angular angle of 110°. And different rows represent different slices. The display window is [-600, 600].

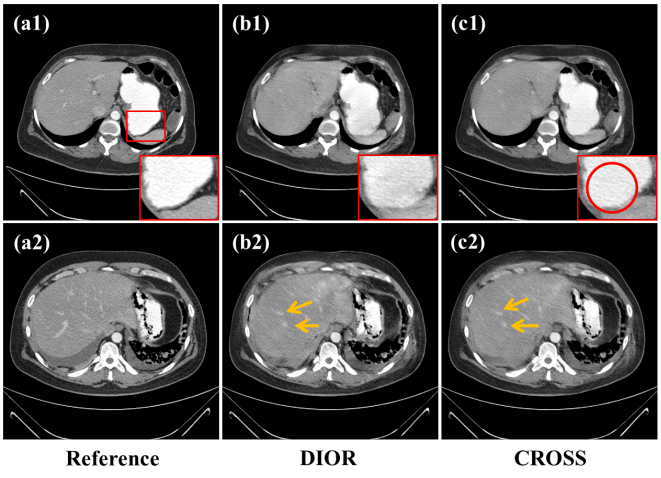

Fig. 8. Reconstruction results from the simulated dataset with the scanning angular range of 90°. The display window is [-160, 240] HU.

[0,110°] was performed to assess various methods.

Fig. 7 shows the selected reconstruction images between different algorithms. For better visual observation, all the images in Fig. 7 were cropped to the size of 448×448. All the DL-based methods can generate high-quality images with fewer artifacts than the FDK algorithm. Moreover, in comparison approaches, DDNet produces better results in edge preservation (as indicated by the yellow arrow in Fig. 7(d2)). From the red arrows in Fig. 7(f1)-(f4), the proposed CROSS framework outperforms other DL-based methods in tissue restoration and detail preservation.

C. *Comparison Between CROSS and DIOR*

Deep iterative reconstruction methods have been applied for limited-angle CT and achieved superior performance to traditional DL-based methods [43, 44, 47]. To compare the deep iterative method and the proposed method, additional experiments were conducted from the simulated dataset with the scanning angular range of 90°. The DIOR [47] was employed as the representative deep iterative method, which adopted the CNN model as the regularization function in the residual space to improve the image quality via the iterative process.

Fig. 8 demonstrates the reconstructed results of the DIOR and CROSS methods. Both the DIOR and CROSS perform well in artifact removal and tissue restoration (as pointed out by the yellow arrows in Fig. 8(b2)(c2)). In addition, the CROSS framework can restore accurate structural features (as marked by the red circle in Fig. 8(c1)). To sum up, the proposed method can obtain competitive results with DIOR, which proves that the multi-domain-based strategy in CROSS is effective for limited-angle CT.

D. *Computational Cost*

Table II lists the computational cost of various methods. All the time was computed based on the simulated dataset with 200 images and a scanning angular range of 110°. MSWDNet and

DDNet are single-domain-based methods that take the least time. IR-based methods (DCAR and DIOR) consume much longer time than other algorithms. Because of three networks and one forward-backward operation, the proposed method spends more time than MSWDNet and DDNet. However, compared to DIOR, CROSS can bring similar results within an appropriate time.

Table II
COMPUTATIONAL COST BETWEEN THE MSWDNET, DDNET, DIOR AND CROSS METHODS (UNIT: SECOND)

Method	MSWDNet	DDNet	DCAR	DIOR	CROSS
Time	8.2	6.9	140.0	2667.0	39.1

Table III
QUANTITATIVE EVALUATIONS FOR THE ABLATION STUDY

Metric	Baseline	SS-Net	+DC+ID-Net	+LDC+ID-Net	CROSS
PSNR	337.37	37.63	38.06	38.73	**39.40**
SSIM	0.9500	0.9522	0.9646	0.9661	**0.9683**

E. Ablation Study

In this section, an ablation study was performed to probe the effects of different modules of the proposed CROSS framework based on the simulated data with the scanning angular range of 90°.

The FED-INet [47] was taken as the baseline model. Then the structure enhancement module was added to the baseline to establish the first comparison model (SS-Net). Next, the data consistency (DC) with $y_3 = y \oplus y_1$ and the image-domain network (ID-Net) was introduced to the first comparison model to build the second comparison model. Moreover, unlike the second comparison, the learned data consistency (LDC) in Eq. (1) with ResNet was employed to create the third comparison model. Last, the residual data consistency in Eq. (2) and the residual-space-based network were adopted to construct the fourth comparison model, i.e., CROSS.

Table III gives the quantitative evaluations of the progressive ablation study. It can be observed that the SS-Net brings higher scores than the baseline model in terms of PSNR, and SSIM because the structure enhancement sub-network could strengthen tissue preservation. Meanwhile, with the assistance of DC and ID-Net, the third model further promotes the reconstructed results both in CT values and image features. Replacing the DC with the learned DC, the fourth model can enhance the data consistency constraint and lead to improvements in all assessments. Notably, the proposed CROSS method gains the best evaluations in all comparison models, claiming the validity of the RDC and residual-space processing.

Besides, to explore the mechanism of different components in CROSS, the reconstructed results of various comparison models are demonstrated. The baseline model can restore most tissue features and remove artifacts, which has been validated in [47]. With the aid of the structure enhancement module, SS-Net performs better in detail restoration (as indicated by the red circle in Fig. 9(c)). However, the third model introduces some uneven artifacts into the reconstructed images (as shown by the blue arrows in Fig. 9(d)), which may be caused by the inaccuracy of DC. After applying an additional ResNet in the projection domain, the fourth model can overcome the drawback of the previous model and lead to better results in edge preservation (as pointed out by the green arrow in Fig. 9(e)). Last, CROSS generates the most impressive images, specifically for the area with larger attenuation coefficients (as demonstrated by the yellow ellipse in Fig. 9(f)).

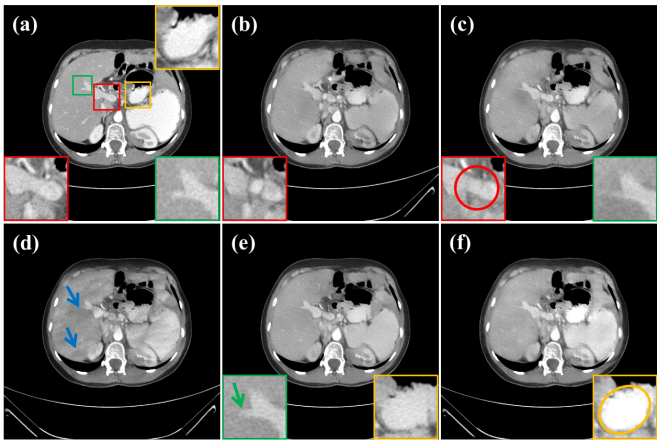

Fig. 9. Simulated dataset reconstruction results of different modules with the scanning angular range of 90°. (a) Reference (b) Baseline model (c) SS-Net. (d) +DC+ID-Net. (e) +LDC+ID-Net. (f) CROSS. The display window is [-240, 160] HU.

IV. CONCLUSION AND DISCUSSION

Deep iterative reconstruction methods have shown remarkable superiority over existing methods [43, 44, 47]. However, these methods often encounter two issues when being applied to practical cone-beam CT imaging, which is memory limitations [43, 44] and longer running time [47]. Meanwhile, hybrid-domain-based methods can also produce high-quality results [33, 61] and be easily used for 3D imaging within an appropriate time. Therefore, based on the hybrid-domain methods, we develop a cross-domain residual-optimization-based structure strengthening reconstruction for limited-angle CT to generate similar results with deep iterative methods. Different from [33], our CROSS framework alternatively utilizes the networks to improve CT images on the image domain and projection domain. Besides, the residual-space-based processings can further improve CROSS in tissue restoration. In addition, the utilization of the structure enhancement module also results in the promotion of the reconstructed images. Both the simulated and real datasets are performed with different scanning angular ranges to validate the proposed method. Compared to existing methods, the CROSS framework performs well in artifact reduction and edge preservation.

There are some similar works to the proposed method. For instance, to overcome the instabilities of deep learning, Wu *et al.* proposed an ACID framework with a combination of deep learning and compressed sensing theory [37, 38]. The key idea of ACID is to employ the pre-trained network to constrain the residual image. Inspired by it, more advanced works have been developed for sparse-view CT [39, 40]. The RDC used in the proposed method was also inspired by ACID and applied to limited-angle CT. However, to further improve edge preservation, our proposed method adopts a more effective structure-strengthening network.

Although the CROSS method demonstrates encouraging improvement in limited-angle CT reconstruction, some issues are still to be noticed. First, the texture extraction used in SS-Net is might not the optimal scheme. Therefore, how constructing the texture and detail map of CT images is still an opening problem. Second, the residual data consistency brings improvements for CROSS. However, it still exists some errors to evaluate the distance between reconstructed images and the ground truth in the projection domain. It remains a challenging problem to effectively ensure data consistency. Last, the noise will be enlarged in SS-Net due to the structure extraction, which may negatively affect the performance of the proposed method. So, how to avoid noise amplification in CROSS should be noticed.

Deep-learning-based methods have demonstrated superior performance than traditional reconstruction methods in the limited-angle CT problem. Nevertheless, most of these methods focus on simulated data or preclinical data, which cannot convincingly validate their practicability in real cases. Therefore, it still has a long way to apply deep learning methods to clinical limited-angle imaging.

ACKNOWLEDGMENTS

All authors declare that they have no known conflicts of interest in terms of competing financial interests or personal relationships that could have an influence or are relevant to the work reported in this paper.

REFERENCES

[1] G. Wang, H. Yu, and B. De Man, "An outlook on x-ray CT research and development," *Medical physics*, vol. 35, no. 3, pp. 1051-1064, 2008.

[2] G. Bachar, J. Siewerdsen, M. Daly *et al.*, "Image quality and localization accuracy in C-arm tomosynthesis-guided head and neck surgery," *Medical physics*, vol. 34, no. 12, pp. 4664-4677, 2007.

[3] H. Gao, L. Zhang, Z. Chen *et al.*, "Direct filtered-backprojection-type reconstruction from a straight-line trajectory," *Optical Engineering*, vol. 46, no. 5, pp. 057003, 2007.

[4] A. Tingberg, "X-ray tomosynthesis: a review of its use for breast and chest imaging," *Radiation protection dosimetry*, vol. 139, no. 1-3, pp. 100-107, 2010.

[5] D. A. Jaffray, J. H. Siewerdsen, J. W. Wong *et al.*, "Flat-panel cone-beam computed tomography for image-guided radiation therapy," *International Journal of Radiation Oncology*Biology*Physics*, vol. 53, no. 5, pp. 1337-1349, 2002.

[6] D. Van de Sompel, and M. Brady, "A systematic performance analysis of the simultaneous algebraic reconstruction technique (SART) for limited angle tomography," in *2008 30th Annual International Conference of the IEEE Engineering in Medicine and Biology Society*, 2008, pp. 2729-2732.

[7] D. Hu, W. Wu, M. Xu *et al.*, "SISTER: Spectral-Image Similarity-Based Tensor With Enhanced-Sparsity Reconstruction for Sparse-View Multi-Energy CT," *IEEE Transactions on Computational Imaging*, vol. 6, pp. 477-490, 2020.

[8] W. Wu, D. Hu, K. An *et al.*, "A High-Quality Photon-Counting CT Technique Based on Weight Adaptive Total-Variation and Image-Spectral Tensor Factorization for Small Animals Imaging," *IEEE Transactions on Instrumentation and Measurement*, vol. 70, pp. 1-14, 2021.

[9] E. Y. Sidky, C.-M. Kao, and X. Pan, "Accurate image reconstruction from few-views and limited-angle data in divergent-beam CT," *Journal of X-Ray Science and Technology*, vol. 14, pp. 119-139, 2006.

[10] Z. Chen, X. Jin, L. Li *et al.*, "A limited-angle CT reconstruction method based on anisotropic TV minimization," *Physics in Medicine & Biology*, vol. 58, no. 7, pp. 2119, 2013.

[11] T. Wang, K. Nakamoto, H. Zhang *et al.*, "Reweighted Anisotropic Total Variation Minimization for Limited-Angle CT Reconstruction," *IEEE Transactions on Nuclear Science*, vol. 64, no. 10, pp. 2742-2760, 2017.

[12] Y. Huang, O. Taubmann, X. Huang *et al.*, "Scale-Space Anisotropic Total Variation for Limited Angle Tomography," *IEEE Transactions on Radiation and Plasma Medical Sciences*, vol. 2, no. 4, pp. 307-314, 2018.

[13] W. Wu, Y. Zhang, Q. Wang *et al.*, "Low-dose spectral CT reconstruction using image gradient ℓ0–norm and tensor dictionary," *Applied Mathematical Modelling*, vol. 63, pp. 538-557, 2018.

[14] Y.-L. Sun, and J.-X. Tao, "Image reconstruction from few views by ℓ0-norm optimization," *Chinese Physics B*, vol. 23, no. 7, pp. 078703, 2014.

[15] C. Wang, and L. Zeng, "Error bounds and stability in the L0 regularized for CT reconstruction from small projections," *Inverse Problems Imaging*, vol. 10, no. 3, pp. 829, 2016.

[16] M. Xu, D. Hu, F. Luo *et al.*, "Limited-Angle X-Ray CT Reconstruction Using Image Gradient ℓ₀-Norm With Dictionary Learning," *IEEE Transactions on Radiation and Plasma Medical Sciences*, vol. 5, no. 1, pp. 78-87, 2021.

[17] W. Wu, Q. Wang, F. Liu *et al.*, "Block matching frame based material reconstruction for spectral CT," *Physics in Medicine & Biology*, vol. 64, no. 23, pp. 235011, 2019.

[18] W. Wu, F. Liu, Y. Zhang *et al.*, "Non-Local Low-Rank Cube-Based Tensor Factorization for Spectral CT Reconstruction," *IEEE Transactions on Medical Imaging*, vol. 38, no. 4, pp. 1079-1093, 2019.

[19] J. Liu, J. Ma, Y. Zhang *et al.*, "Discriminative feature representation to improve projection data inconsistency for low dose CT imaging," *IEEE Transactions on Medical Imaging*, vol. 36, no. 12, pp. 2499-2509, 2017.

[20] S. Wang, H. Yu, Y. Xi *et al.*, "Spectral-Image Decomposition With Energy-Fusion Sensing for Spectral CT Reconstruction," *IEEE Transactions on Instrumentation and Measurement*, vol. 70, pp. 1-11, 2021.

[21] D. Hu, Y. Zhang, J. Zhu *et al.*, "TRANS-Net: Transformer-enhanced Residual-error AlterNative Suppression Network for MRI Reconstruction," *IEEE Transactions on Instrumentation and Measurement*, pp. 1-1, 2022.

[22] Z. Huang, J. Zhang, Y. Zhang *et al.*, "DU-GAN: Generative Adversarial Networks With Dual-Domain U-Net-Based Discriminators for Low-Dose CT Denoising," *IEEE Transactions on Instrumentation and Measurement*, vol. 71, pp. 1-12, 2022.

[23] Y. Zhang, D. Hu, Z. Yan *et al.*, "TIME-Net: Transformer-Integrated Multi-Encoder Network for limited-angle artifact removal in dual-energy CBCT," *Medical Image Analysis*, vol. 83, pp. 102650, 2023.

[24] Y. Zhang, D. Hu, Q. Zhao *et al.*, "CLEAR: Comprehensive Learning Enabled Adversarial Reconstruction for Subtle Structure Enhanced Low-Dose CT Imaging," *IEEE Transactions on Medical Imaging*, vol. 40, no. 11, pp. 3089-3101, 2021.

[25] D. Hu, Y. Zhang, J. Liu *et al.*, "PRIOR: Prior-Regularized Iterative Optimization Reconstruction for 4D CBCT," *IEEE Journal of Biomedical and Health Informatics*, pp. 1-12, 2022.

[26] Y. Zhang, T. Lv, R. Ge *et al.*, "CD-Net: Comprehensive Domain Network With Spectral Complementary for DECT Sparse-View Reconstruction," *IEEE Transactions on Computational Imaging*, vol. 7, pp. 436-447, 2021.

[27] Y. Zhang, D. Hu, S. Hao *et al.*, "DREAM-Net: Deep Residual Error Iterative Minimization Network for Sparse-View CT Reconstruction," *IEEE Journal of Biomedical and Health Informatics*, vol. 27, no. 1, pp. 480-491, 2023.

[28] J. Gu, and J. C. Ye, "Multi-Scale Wavelet Domain Residual Learning for Limited-Angle CT Reconstruction," in *Fully Three-Dimensional Image Reconstruction in Radiology and Nuclear Medicine*, 2017.

[29] L. Ziheng, Z. Wenkun, W. Linyuan *et al.*, "A sinogram inpainting method based on generative adversarial network for limited-angle computed tomography," in *SPIE*, 2019, pp. 1107220.

[30] R. Anirudh, H. Kim, J. J. Thiagarajan *et al.*, "Lose the views: Limited angle CT reconstruction via implicit sinogram completion," in *Proceedings of the IEEE Conference on Computer Vision and Pattern Recognition*, 2018, pp. 6343-6352.

[31] T. Würfl, M. Hoffmann, V. Christlein *et al.*, "Deep Learning Computed Tomography: Learning Projection-Domain Weights From Image Domain in Limited Angle Problems," *IEEE Transactions on Medical Imaging*, vol. 37, no. 6, pp. 1454-1463, 2018.

[32] Y. Huang, A. Preuhs, G. Lauritsch *et al.*, "Data Consistent Artifact Reduction for Limited Angle Tomography with Deep Learning Prior," in

Machine Learning for Medical Image Reconstruction, Cham, 2019, pp. 101-112.
[33] D. Hu, Y. Zhang, J. Liu *et al.*, "SPECIAL: Single-Shot Projection Error Correction Integrated Adversarial Learning for Limited-Angle CT," *IEEE Transactions on Computational Imaging*, vol. 7, pp. 734-746, 2021.
[34] Q. Zhang, Z. Hu, C. Jiang *et al.*, "Artifact removal using a hybrid-domain convolutional neural network for limited-angle computed tomography imaging," *Physics in Medicine & Biology*, vol. 65, no. 15, pp. 155010, 2020.
[35] F. Jiao, Z. Gui, K. Li *et al.*, "A Dual-Domain CNN-Based Network for CT Reconstruction," *IEEE Access*, vol. 9, pp. 71091-71103, 2021.
[36] B. Zhou, X. Chen, H. Xie *et al.*, "DuDoUFNet: Dual-Domain Under-to-Fully-Complete Progressive Restoration Network for Simultaneous Metal Artifact Reduction and Low-Dose CT Reconstruction," *IEEE Transactions on Medical Imaging*, vol. 41, no. 12, pp. 3587-3599, 2022.
[37] W. Wu, D. Hu, W. Cong *et al.*, "Stabilizing deep tomographic reconstruction: Part A. Hybrid framework and experimental results," *Patterns*, vol. 3, no. 5, pp. 100474, 2022.
[38] W. Wu, D. Hu, W. Cong *et al.*, "Stabilizing deep tomographic reconstruction: Part B. Convergence analysis and adversarial attacks," *Patterns*, vol. 3, no. 5, pp. 100475, 2022.
[39] W. Wu, D. Hu, C. Niu *et al.*, "DRONE: Dual-Domain Residual-based Optimization NEtwork for Sparse-View CT Reconstruction," *IEEE Transactions on Medical Imaging*, vol. 40, no. 11, pp. 3002-3014, 2021.
[40] W. Wu, X. Guo, Y. Chen *et al.*, "Deep Embedding-Attention-Refinement for Sparse-view CT Reconstruction," *IEEE Transactions on Instrumentation and Measurement*, pp. 1-1, 2022.
[41] K. Zhang, Y. Li, W. Zuo *et al.*, "Plug-and-Play Image Restoration with Deep Denoiser Prior," *IEEE Transactions on Pattern Analysis and Machine Intelligence*, pp. 1-1, 2021.
[42] J. Sun, H. Li, and Z. Xu, "Deep ADMM-Net for compressive sensing MRI," in *Advances in neural information processing systems*, 2016.
[43] W. Cheng, Y. Wang, H. Li *et al.*, "Learned Full-Sampling Reconstruction From Incomplete Data," *IEEE Transactions on Computational Imaging*, vol. 6, pp. 945-957, 2020.
[44] B. Zhou, S. K. Zhou, J. S. Duncan *et al.*, "Limited View Tomographic Reconstruction Using a Cascaded Residual Dense Spatial-Channel Attention Network With Projection Data Fidelity Layer," *IEEE Transactions on Medical Imaging*, vol. 40, no. 7, pp. 1792-1804, 2021.
[45] C. Chen, Y. Xing, H. Gao *et al.*, "Sam's Net: A Self-Augmented Multi-Stage Deep-Learning Network for End-to-End Reconstruction of Limited Angle CT," *IEEE Transactions on Medical Imaging*, pp. 1-1, 2022.
[46] J. Wang, L. Zeng, C. Wang *et al.*, "ADMM-based deep reconstruction for limited-angle CT," *Physics in Medicine & Biology*, vol. 64, no. 11, pp. 115011, 2019.
[47] D. Hu, Y. Zhang, J. Liu *et al.*, "DIOR: Deep Iterative Optimization-Based Residual-Learning for Limited-Angle CT Reconstruction," *IEEE Transactions on Medical Imaging*, vol. 41, no. 7, pp. 1778-1790, 2022.
[48] Z. Zhang, X. Liang, X. Dong *et al.*, "A Sparse-View CT Reconstruction Method Based on Combination of DenseNet and Deconvolution," *IEEE Transactions on Medical Imaging*, vol. 37, no. 6, pp. 1407-1417, 2018.
[49] C. Ma, Y. Rao, J. Lu *et al.*, "Structure-Preserving Image Super-Resolution," *IEEE Transactions on Pattern Analysis and Machine Intelligence*, pp. 1-1, 2021.
[50] C. Wang, H.-Z. Shen, F. Fan *et al.*, "EAA-Net: A novel edge assisted attention network for single image dehazing," *Knowledge-Based Systems*, vol. 228, pp. 107279, 2021.
[51] Q. Cai, J. Li, H. Li *et al.*, "TDPN: Texture and Detail-Preserving Network for Single Image Super-Resolution," *IEEE Transactions on Image Processing*, vol. 31, pp. 2375-2389, 2022.
[52] K. He, X. Zhang, S. Ren *et al.*, "Deep residual learning for image recognition," in *Proceedings of the IEEE Conference on Computer Vision and Pattern Recognition*, 2016, pp. 770-778.
[53] K. Zhang, W. Zuo, Y. Chen *et al.*, "Beyond a Gaussian Denoiser: Residual Learning of Deep CNN for Image Denoising," *IEEE Transactions on Image Processing*, vol. 26, no. 7, pp. 3142-3155, 2017.
[54] J. Schlemper, J. Caballero, J. V. Hajnal *et al.*, "A Deep Cascade of Convolutional Neural Networks for Dynamic MR Image Reconstruction," *IEEE Transactions on Medical Imaging*, vol. 37, no. 2, pp. 491-503, 2018.
[55] H. Gupta, K. H. Jin, H. Q. Nguyen *et al.*, "CNN-Based Projected Gradient Descent for Consistent CT Image Reconstruction," *IEEE Transactions on Medical Imaging*, vol. 37, no. 6, pp. 1440-1453, 2018.
[56] Q. Yang, P. Yan, Y. Zhang *et al.*, "Low-Dose CT Image Denoising Using a Generative Adversarial Network With Wasserstein Distance and Perceptual Loss," *IEEE Transactions on Medical Imaging*, vol. 37, no. 6, pp. 1348-1357, 2018.
[57] K. Simonyan, and A. Zisserman, "Very deep convolutional networks for large-scale image recognition," *arXiv:1409.1556*, 2014.
[58] D. P. Kingma, and J. Ba, "Adam: A method for stochastic optimization," *arXiv:1412.6980*, 2014.
[59] A. Biguri, M. Dosanjh, S. Hancock *et al.*, "TIGRE: a MATLAB-GPU toolbox for CBCT image reconstruction," *Biomedical Physics & Engineering Express*, vol. 2, no. 5, pp. 055010, 2016.
[60] W. Zhou, A. C. Bovik, H. R. Sheikh *et al.*, "Image quality assessment: from error visibility to structural similarity," *IEEE Transactions on Image Processing*, vol. 13, no. 4, pp. 600-612, 2004.
[61] X. Yin, Q. Zhao, J. Liu *et al.*, "Domain Progressive 3D Residual Convolution Network to Improve Low-Dose CT Imaging," *IEEE Transactions on Medical Imaging*, vol. 38, no. 12, pp. 2903-2913, 2019.